Research Article

Zhu Yu-Jie, Ma Jing-Ling*, Wang Guang-Xin, Song Ke-Xing, and Heinz Rolf Stock

Corrosion behaviour of multilayer CrN coatings deposited by hybrid HIPIMS after oxidation treatment

https://doi.org/10.1515/ntrev-2020-0048
received May 11, 2020; accepted June 6, 2020

Abstract: Chromium nitride coatings prepared by physical vapour deposition (PVD) show high hardness, high strength and good thermal conductivity, which makes them useful for cutting and forming tools. In this article, the microstructure and corrosion resistance of multilayer Cr/CrN coatings deposited by arc evaporation and hybrid high power impulse magnetron sputtering (hybrid HIPIMS) after oxidation between 500 and 800°C were examined. The average thickness of the coatings was about 3.5 μm. By means of the surface morphology analysis, elemental energy spectrometry and potentiodynamic polarization tests, the performances of the two groups of coatings have been compared. The results revealed that the coating deposited by the hybrid HIPIMS has stronger binding force with substrate, fewer surface defects and a denser structure. Also, the hybrid HIPIMS coatings have a better oxidation resistance and a better corrosion resistance compared to the arc evaporated coatings.

Keywords: arc evaporation, hybrid HIPIMS, Cr/CrN coating, oxidation, corrosion resistance, potentiodynamic polarization test

*** Corresponding author: Ma Jing-Ling,** School of Materials Science and Engineering, Henan University of Science and Technology, Luoyang 471023, China; Research Center for High Purity Materials, Henan University of Science and Technology, Luoyang 471023, China, e-mail: zyjmiaohome@163.com
Zhu Yu-Jie, Song Ke-Xing: School of Materials Science and Engineering, Henan University of Science and Technology, Luoyang 471023, China
Wang Guang-Xin, Heinz Rolf Stock: School of Materials Science and Engineering, Henan University of Science and Technology, Luoyang 471023, China; Research Center for High Purity Materials, Henan University of Science and Technology, Luoyang 471023, China

1 Introduction

Magnetron sputtering and cathodic arc deposition are the most popular technologies in physical vapour deposition. The main advantages of the magnetron sputtering are the relatively low coating temperature, low surface roughness of the coating and very few droplets inside the coating [1,2]. Therefore, the magnetron sputtering has been widely used in industrial production [3,4]. Main disadvantage of direct current magnetron sputtering (DCMS) is the low ionization ratio of the sputtered atoms. This can cause insufficient bond strength between the coating and the substrate. Compared with the sputtering, the surface roughness of the coating deposited by the cathode arc is slightly higher, but it has a higher ionization rate in the deposition process, and the coating prepared by cathode arc deposition has a stronger coating base bonding strength [5]. Currently, the market share of cathodic arc deposition technology in the coating of cemented carbide tools is far greater than other coating technologies. In summary, after years of development, the two more mature physical vapour deposition (PVD) coating technologies still have some drawbacks.

A new development in sputtering is high power impulse magnetron sputtering (HIPIMS) [6]. Compared with DCMS, HIPIMS can generate very high current pulse, equivalent to more than 1,000 times of DCMS, thereby achieving an ionization rate of more than 50%, making it possible to prepare higher quality coating [7]. HIPIMS effectively solved the shortcomings of traditional physical vapour deposition (DCMS) such as poor interface adhesion, low surface quality and poor uniformity, but its deposition rate was greatly reduced. Compared with DCMS, it is an important obstacle for HIPIMS to become an industrial application. Sarakinos et al. [8] compared the deposition rates of HIPIMS and DCMS in a review, and the results showed that Ti deposition rates in HIPIMS were 25–85% lower than that in the DCMS process. Meanwhile, Cr only accounts for 29% of DCMS deposition rate, Cu accounts for 37–80%, Al accounts for 35%, Ta accounts for 20–40%,

Zr accounts for 15% and Al_2O_3 accounts for 25–31%. In recent years, researchers have found that the deposition rate can be improved by enhancing the discharge performance of HIPIMS, so as to make full use of its advantages. Therefore, the coating was prepared by using HIPIMS assisted by bipolar pulsed magnetron sputtering (BIPPMS).

In the field of metal processing and surface strengthening, CrN-based coatings have become a research hotspot nowadays due to their excellent mechanical properties, high temperature oxidation resistance, good wear resistance and corrosion resistance. In the past 10 years, researchers deposited hard CrN-based coatings with good mechanical properties and high-temperature oxidation resistance. Especially in recent years, many researchers at home and abroad have prepared Cr/CrN multilayer film as a bilayer and discussed the influence of the bilayer period on the coating performance. Jin et al. prepared CrN coatings and three CrN multilayer coatings with different periods on monocrystalline silicon by magnetron sputtering. It is confirmed that the hardness and indentation plasticity of the multilayer coatings are better than those of the monolayer layer coatings, and both increase with the decrease in the bilayer period [9]. Lin et al. introduced a novel multipulse modulation pulsed power magnetron sputtering technique for depositing nanostructured layered CrN films. They concluded that the structure and performance of the modulated pulsed power magnetron sputtering CrN film depended on the pulse repetition time. At the same time, a film with a maximum hardness of 30.5 GPa was obtained [10]. Song et al. deposited Cr/CrN multilayer coatings with a bilayer period of 260–1351 nm on 304 stainless steel substrate by a method of arc ion plating. The hardness and elastic modulus of the multilayer coatings were analysed and discussed. It is found that the indentation toughness of the multilayer coating is related to the bilayer period, and the Cr/CrN multilayer coating with a proper thickness of the Cr layer and the nitride layer has the highest indentation toughness [11]. According to the study by Lamastra et al., X-ray diffraction (XRD) was used to test the residual stress of CrN/Cr/CrN multilayer coatings generated by arc ion plating on three different steel substrates. No matter what type of steel is used as the substrate, the residual CrN layer has a residual pressure and the results reveal stress anisotropy in the coating plane [12].

However, it is worth discussing whether CrN coating can maintain its excellent performance under some harsh working conditions. On one hand, more and more people are gradually realizing that the coating only made by HIPIMS has a low deposition rate although the coating quality is excellent. Therefore, the hybrid HIPIMS technology (HIPIMS assisted by one or more other physical vapour deposition methods) to deposit coatings has gradually become a research hotspot in recent years. On the other hand, arc ion plating technology is a completely different method from HIPIMS technology, and its wide applicability is well worth comparing. At the same time, multilayer CrN coating can effectively improve the performance of the coating and can be used as a research object.

Therefore, in this article, CrN-based coatings were used as research objects. Two groups of coatings were prepared by cathodic arc deposition and by HIPIMS assisted by BIPPMS. Phase transitions and microstructure evolutions of the CrN coatings oxidation were observed, and the process and its effect on high temperature oxidation and corrosion resistance were studied.

2 Experimental

2.1 Coating deposition

CrN coatings were fabricated by a semi-industrial PVD unit equipped with six cathodic arc ion evaporators (4G-CAE1028B) and Hüttinger magnetron sputtering sources: two bipolar power supplies, a high pulse power supply and a DC bias supply. Coating A was deposited by arc evaporation, and Coating B was prepared by Hüttinger magnetron sputtering sources. The deposition of Cr/CrN multilayer coatings onto 304 stainless steel substrates with a diameter of 40 mm was conducted in this system. The chromium targets used to deposit both groups of coatings has a purity of 99.9%.

Before deposition, the substrates were mirror polished, ultrasonically cleaned in an acetone solution and an industrial anhydrous ethanol reagent and dried. The coating process was carried out in a vertical cylinder vacuum chamber with an effective coating space of φ 600 mm × 600 mm.

The samples were clamped on a rotating carousel with a rotation speed of $2\,\mathrm{min}^{-1}$. To remove oxygen, the deposition chamber was pumped down to a base pressure of 5×10^{-4} Pa and heated up to 400°C. Then, the pressure was increased to 2 Pa by argon supply and a sputter cleaning of the substrates with argon and chromium ions at a bias voltage of –1,000 V and a high pulse power of 10 kW for 15 min.

Deposition of coating A was performed at the substrate bias voltage of –40 V and an arc current of 120 A under a nitrogen–argon atmosphere at 7 Pa. The

deposition time of each layer was controlled at 920 s. During deposition of coating B, the pressure was kept at 0.55 Pa (33% nitrogen and 67% argon), and the pulse width was set to 100 μs for HIPIMS and 2 μs for BIPPMS. Both the bipolar power and the high pulse power were adjusted to 8 kW. The frequency of the bipolar pulse unit is 40 kHz. Multilayer coatings were deposited by superimposing alternating layers of Cr and CrN. Each layer was deposited for 900 s, and a total of six layers are deposited with −60 V substrate bias voltages. The main experimental parameters are presented in Table 1.

2.2 Coating characterization

The thickness of the coatings and the different layers were evaluated by ball crater tests (SuPro Instruments). The sample and the ball (a ball bearing steel) with a diameter of 30 mm were ground for 90 s with a diamond suspension liquid. The coating thickness is calculated using a simple geometrical equation [13].

The adhesion of the coatings was characterized by the well-known Rockwell C indentation test prescribed by the VDI 3198 norm, as a destructive quality test for coated compounds. This simple low-cost test can qualitatively characterize the adhesion of the coating to the substrate [14]. The principle is that the tapered diamond indenter penetrates the surface of the coating, causing plastic deformation of the substrate and fracture of the coating. As with the indentation test, the indentation depth must follow the 1/10 rule, so the total thickness of the specimen must be at least ten times greater than the indentation depth. The coated sample is evaluated by scanning electron microscopy (SEM).

The samples, divided into four groups, were oxidized in a tubular heating device. The four groups of samples were raised from room temperature in air at a rate of 5 K/min to 500, 600, 700 and 800°C. After a holding time of 2 h, the samples were allowed to cool down again.

The surface morphology of the coatings before and after oxidation treatment was observed by field emission scanning electron microscopy (FESEM, JSM-7800F). Energy-dispersive X-ray spectroscopy (EDX) with FESEM was conducted to determine the elemental composition. The phases were examined using an X-ray diffractometer (Bruker-AXS D8 Advance; $U = 40$ kV, $I = 40$ A) with copper Cu Kα radiation ($\lambda = 0.1541$ nm), and a scanning speed of 4°/min.

Table 1: Deposited parameters of Cr/CrN multilayer coatings

Sample	Ar feed (sccm)	N_2 feed (sccm)	Pulse width (μs)	Bipolar/high pulse power (kW)	Arc current (A)	Bias voltage (V)	Temperature (°C)	Deposition time (1 layer) (s)
Coating A	200	100	—	—	120	−40	400	920
Coating B	200	100	100	8	—	−60	400	900

The electrochemical properties of the CrN coatings were tested by means of a three-electrode system in a 3.5 mass% NaCl aqueous solution with a CHI660C Electrochemical Workstation (HuaChen ShangHai, China). The working electrode was the CrN-coated sample inlaid in epoxy resin, and the exposed area was about 1 cm^2. A graphite electrode served as an auxiliary electrode. A saturated calomel electrode (SCE) was used as a reference electrode. The potentiodynamic polarization tests were started after a 1,000 s stabilization period of the samples in the open-circuit conditions, so that a quasi-stable potential was reached. The potentiodynamic polarization curves were carried out at a scan rate of 0.001 V s^{-1} over the potential range from −0.6 to 0 V.

3 Experimental results and discussion

3.1 Thickness and adhesion

Many research groups tried to enhance the adhesion between the CrN coating and the substrate by applying a chromium interlayer with a thickness of 300–400 nm. The transition of the composition is beneficial to reduce the internal stress of the coating. Therefore, to ensure that the composition has a certain gradient, the first layer is always a metal chromium layer. The results of the ball crater test of two typical six-layer coatings by arc evaporation and hybrid HIPIMS are shown in Figure 1. The thickness of coating A and coating B is 3.6 and 3.5 µm, respectively. Thus, the deposition rates of these two coatings are 38 and 40 nm/min, respectively. It can be found that under the parameter settings in this article, the deposition rate of hybrid HIPIMS is equivalent to that of arc evaporation plating, and the deposition rate has been improved.

Figure 2 shows SEM images of coatings A and B of both the surface micromorphology and the Rockwell indentation. The indentation of coating A (Figure 2a) shows some delaminations and some cracks. Compared with coating A, the indentation on the inner wall of coating B (Figure 2b) is relatively uniform with fewer cracks on the edge. Quantification of the appearance according to VDI 3198 [15,16] results in HF.2 and HF.3 (Figure 3), indicating that both coatings meet the requirements. Adhesion between bodies is strongly influenced by surface roughness [17,18].

Figure 2 shows that the surface quality of coating B is superior to that of coating A. The surface of coating A, shown in Figure 2c, reveals large numbers of defects, which include, among others, microdroplets of evaporated material of various sizes and shapes that are formed in the plasma during the coating process. In contrast, the surface of the sputtered coating B (Figure 2d) is dense and shows very few defects. This is typical for sputtering processes and may be connected with the high-power pulses applied here [19,20].

3.2 Composition and phases

The chemical composition of the cross-section of coatings was measured by EDX and is shown in Figure 4. The results reveal that in both cases, multilayer Cr/CrN coatings with a stoichiometric ratio (Cr/N) of nearly 3/1 were obtained. In the meantime, the boundary of the multilayer morphology of the cross-section of coating A is clearly visible, and the interlayer between the coating and the substrate can be observed. In comparison, the famous columnar crystal structure appears in the cross-section of coating B, but the boundary between the layers cannot be easily distinguished.

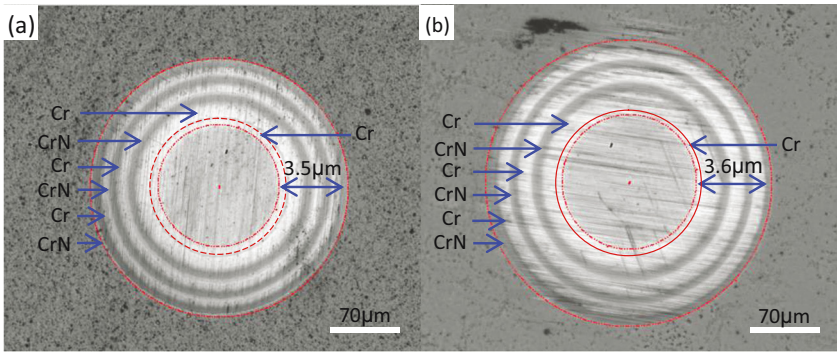

Figure 1: Crater grinding in (a) coating A and (b) coating B.

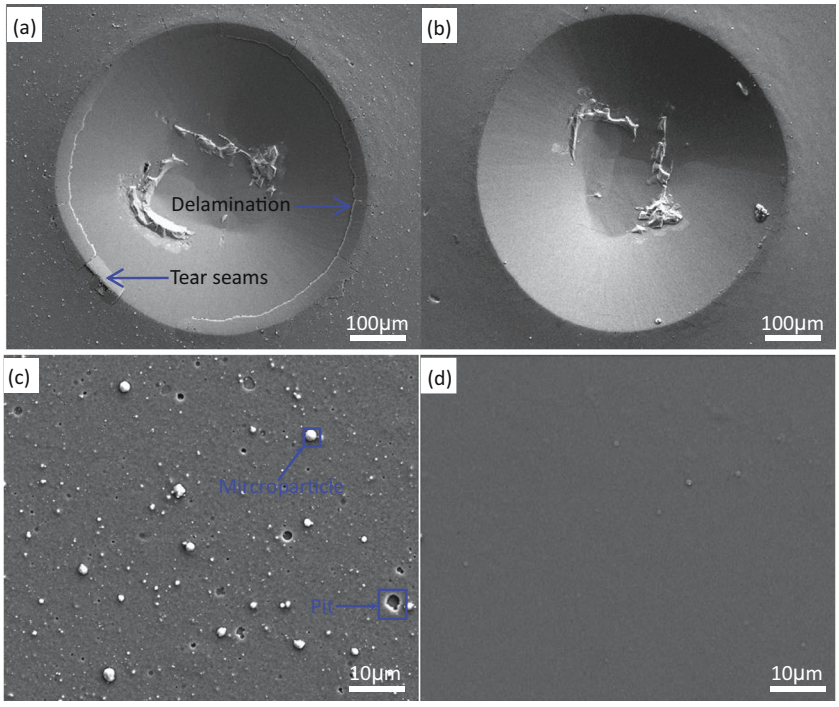

Figure 2: Rockwell indentation and surface microstructure of as-deposited coatings A (a and c) and B (b and d).

The interlayer and the first layer are almost completely melted into one, which further shows its good adhesion.

The XRD patterns of the as-deposited coatings A and B, shown in Figure 5, exhibit a NaCl-type face centre cubic (fcc) structure. Mainly three phases, CrN, Cr and Cr_2N, were found in both coatings. The CrN phase and the Cr phase were the main components of the experimentally designed multilayer coating. The diffraction peaks' orientation of CrN were mainly on the (111), (200) and (311) planes. The preferred orientation of both CrN layers (coatings A and B) was the (200) plane with a strong, sharp and symmetrical diffraction spectrum.

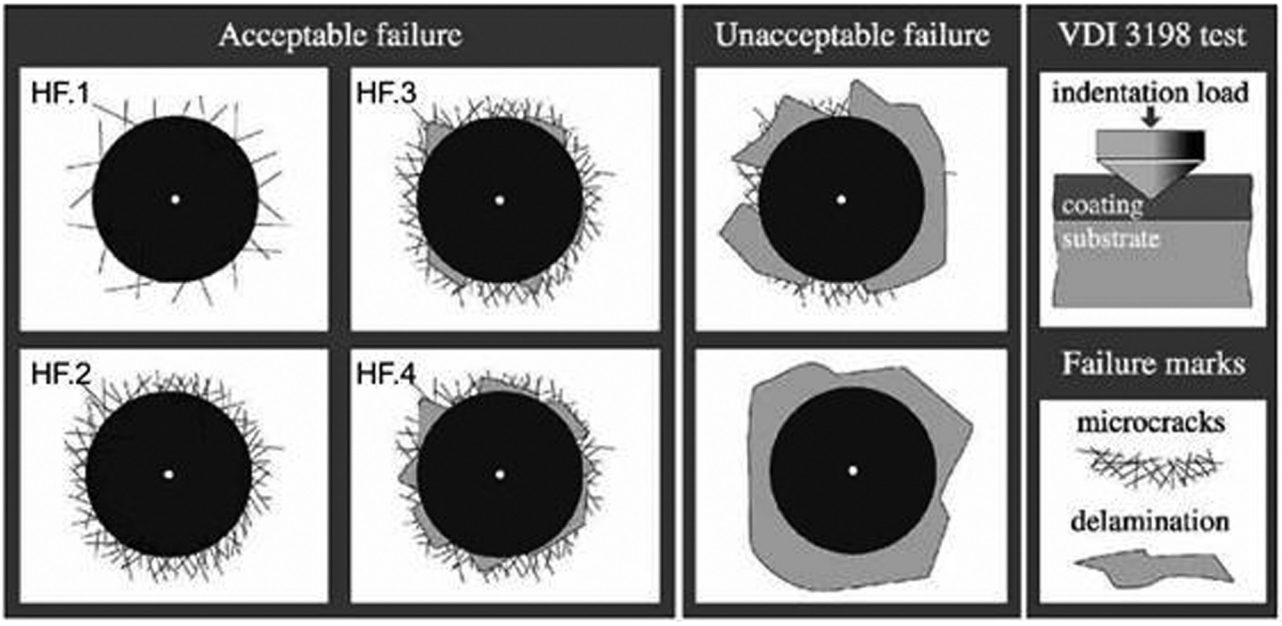

Figure 3: The principle of VDI 3198 indentation test [16].

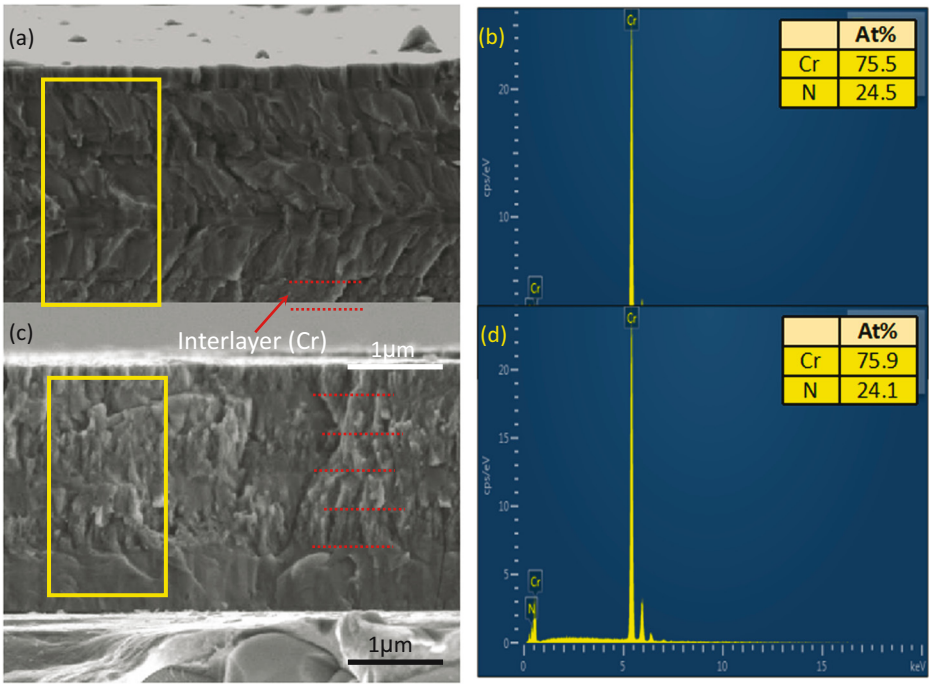

Figure 4: Cross-section morphology and composition structure of coatings A (a and b) and B (c and d).

This proves the good crystallinity and a complete lattice. The preferred orientation of the Cr phase was the (200) plane. The appearance of the Cr_2N phase in the multilayer coatings may be attributed to the fluctuations in the flow rate of nitrogen [21,22]. In principle, under normal conditions, the nitrogen flow rate was sufficient to produce stoichiometric CrN, but in the actual coating process, it took a certain time to reach the nitrogen concentration in the gas phase. The main diffraction peaks of the Cr_2N phase were broad and diffuse, indicating that the crystal grains were very small, combined with defects such as dislocations. This may cause the secondary nucleation and the growth of crystal grains due to the increase of the bias voltage, thereby reducing the half width.

All peaks associated with the Cr and CrN phases were shifted to lower 2-theta values compared to the standard ICCD card [10]. This indicates a state of compressive residual stress due to thermal stress and intrinsic stress [23]. The intrinsic stress is caused by the accumulation of defects, mostly point defects such as vacancies or interstitial atoms, as well as a high dislocation density [21,24]. Thermal stress is mainly due to the difference in the linear thermal expansion coefficient (CTE) between the substrate and the coating after deposition, resulting in a mismatch between the substrate and the coating during the postdeposition cooling. The CTE for CrN is $2.3 \times 10^{-6}\,K^{-1}$, while the CTE for the stainless steel is much larger (around $15 \times 10^{-6}\,K^{-1}$) [23,25].

To investigate the effect of the oxidation test on the corrosion resistance of the coating, both coatings were placed in a tube furnace, internally flowed by air, and oxidized for 2 h at 500, 600, 700 and 800°C. Heating rate was 5 K/min. The chemical compositions of the oxidized coatings' surface at different temperatures are presented in Table 2. With increasing temperature, the content of nitrogen in both coatings decreased significantly, the

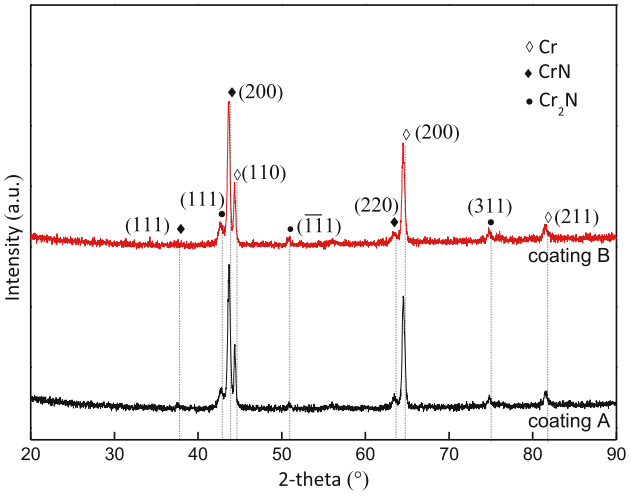

Figure 5: XRD patterns of the as-deposited coating.

Table 2: Chemical compositions of the CrN/N coatings' surface oxidized at different temperatures

Sample	Temperature (°C)	Cr (at%)	N (at%)	O (at%)
Coating A	500	45.9	49.2	4.9
	600	58.9	26.6	14.5
	700	54.8	6.1	39.1
	800	45.3	2.5	52.2
Coating B	500	51.4	39.95	8.38
	600	59.5	20.3	20.2
	700	48.7	13.9	37.5
	800	43.3	1.7	55.0

content of oxygen increased gradually, whereas chromium shows only small changes.

Figure 5 shows the result of the EDX analysis of the cross-section composition of coatings A and B after different temperature treatments. Regardless of the oxidation temperature, it can be found that the boundaries between coatings layers are fused with each other, and the characteristics of columnar crystals disappear. This is because the increase in temperature accelerates the migration of O atoms to the inside and the diffusion of atoms inside the coating, so that the structure inside the coating is rearranged. During low-temperature oxidation (600°C, Figure 6a), the N in the inner layer of coating A diffuses into the outside of the coating and the external O diffuses into the inside of the coating, resulting in high N and O contents near the surface. For coating B, tight columnar crystal structure prevents the migration of the inner N atoms to the outside and the erosion of the outer O atoms to the inside to a certain extent. Finally, when oxidized at 800°C, the O atom diffusion depth of coating B (about 1.5 μm) is smaller than that of coating A (2.5 μm), achieving better oxidation resistance.

It can be seen from the XRD pattern (Figure 7) of coating A that after oxidation at 500°C, the coating contains the phases CrN, Cr_2N and Cr, and both Cr and CrN phases have strong diffraction intensity. At the same time, the diffraction peak appeared to be broadened compared to the

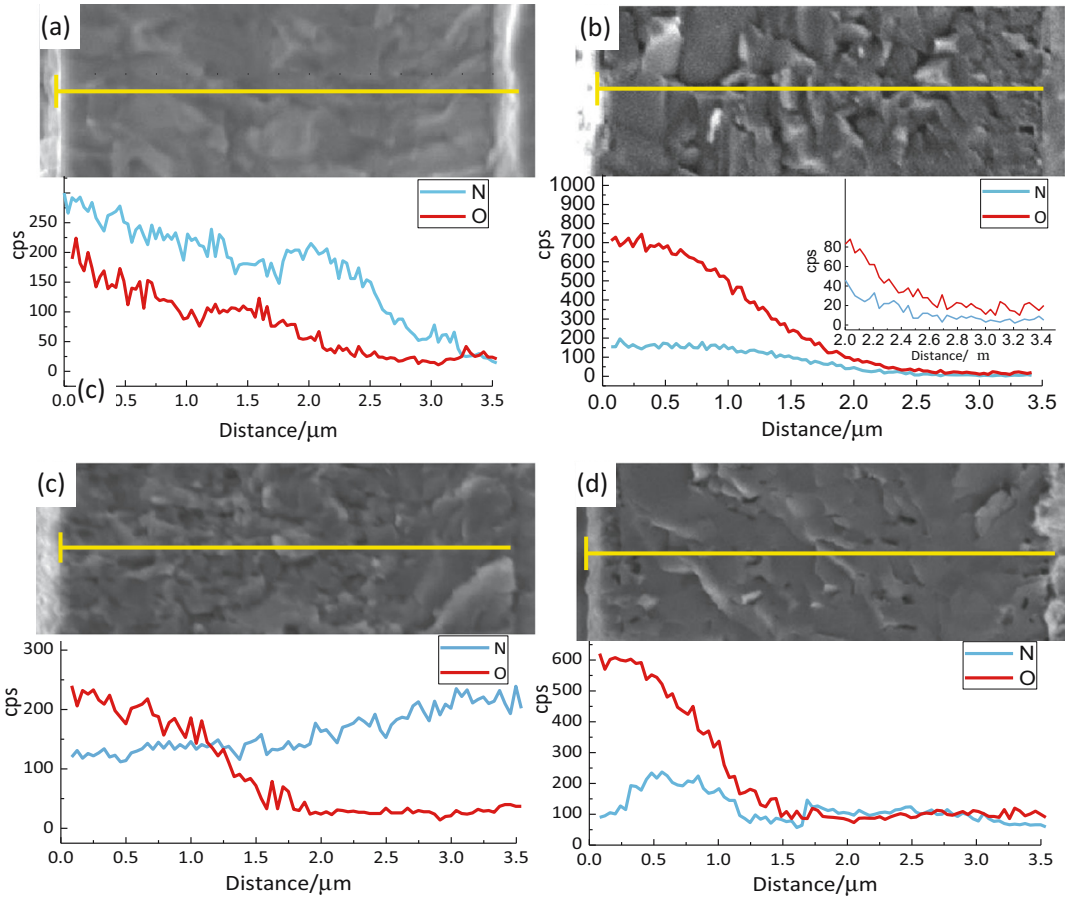

Figure 6: The diffusion depth of nitrogen and oxygen at different temperatures: (a) coating A at 600°C, (b) coating A at 800°C, (c) coating B at 600°C and (d) coating B at 800°C.

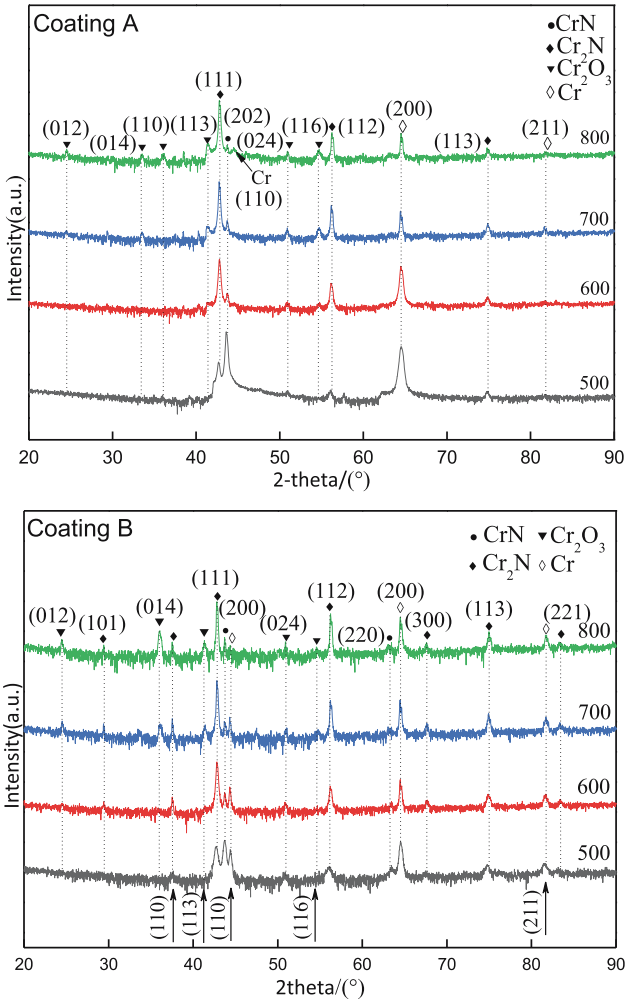

Figure 7: XRD patterns of CrN coatings oxidized at different temperatures.

as-deposited coating, which may be attributed to the incomplete crystal structure caused by the oxidation process. When oxidized at 600°C, the diffraction intensity of the CrN phase was greatly reduced, while the diffraction intensity of Cr_2N was obviously increased. This indicates that the phase structure was changed at the beginning, but no chromium oxide was formed. As the temperature continued to increase, the activity of Cr atoms increased [26].

After oxidation at 700°C, chromium oxide Cr_2O_3, which is the thermodynamically stable compound, can be detected. Possible reactions are as follows [27,28]:

$$\frac{4}{3}\mathrm{CrN} + \mathrm{O_2} = \frac{2}{3}\mathrm{Cr_2O_3} + \frac{2}{3}\mathrm{N_2}, \quad (1)$$

$$\frac{2}{3}\mathrm{Cr_2\,N} + \mathrm{O_2} = \frac{2}{3}\mathrm{Cr_2O_3} + \frac{1}{3}\mathrm{N_2}. \quad (2)$$

The Gibbs free energy changes corresponding to these reactions are as follows [28]:

$$\Delta G(T)R(\mathrm{N_2}) = \Delta G_0 + RT\cdot \ln\left[(p\mathrm{N_2^{2/3}})/(p\mathrm{O_2})\right] = 0.089T - 600.0, \quad (3)$$

$$\Delta G(T)R(\mathrm{N_2}) = \Delta G_0 + RT\cdot \ln\left[(p\mathrm{N_2^{1/3}})/(p\mathrm{O_2})\right] = 0.137T - 670.7. \quad (4)$$

In equations (3) and (4), pO_2 is the partial pressure of oxygen (21% in air), pN_2 is the partial pressure of nitrogen (78% in air), R is the gas constant 8.314 J/kmol, T is the absolute temperature (in K) of the reaction and ΔG_0 is the standard Gibbs free energy for each substance. All the aforementioned data are derived from the NIST-JANAF thermodynamic database. It can be calculated that at 700°C, $\Delta G_R(1)$ is −513 kJ and $\Delta G_R(2)$ is −537 kJ. The XRD patterns of coatings A and B are substantially the same. A significant difference is the two crystal planes (101) and (211) of Cr_2N in coating B. Furthermore, coating B shows a higher intensity of other peaks together with a reduced broadening. Figure 8 shows the surface morphology of coating A, as deposited and oxidized at different temperatures. Figure 8a shows a relatively smooth surface with some microparticles or droplets, which are typical for arc evaporated coatings [29,30]. After oxidation at 500°C, the microparticles did not change much, but on the former smooth surface, a meshwork of lighter line becomes visible. It can be assumed that these areas consist of small oxide particles generated around grain boundaries. Here, the oxidation starts earlier because the energetic status of atoms in the disordered area is higher, and heterogeneous nucleation becomes possible earlier. After oxidation at 600°C, the surface is covered with small-sized (80–240 nm) oxide grains. The majority of the microparticles is still visible. A further increase to 700°C (Figure 8d) allowed the grain size of the oxide crystals to increase to 200–500 nm, and only a few of the microparticles remain visible. Finally, oxidation at 800°C (Figure 8e) allowed the oxide grains to grow up to 500–1,000 nm and then the microparticles disappeared completely.

The surface morphologies of coating B, as deposited and oxidized, are shown in Figure 9. The surface structure of coating B at 10,000 times magnification, as shown in Figure 9(a), was a agglomerated structure, and the surface was smooth without the appearance of microparticles (Figure 2(d)). At the same time, there was no droplet splash during the sputtering process, and the coating structure was uniform.

After heat treatment at 500°C, only a small amount of oxidation becomes visible (Figure 9b). At higher magnification, fine oxide crystals can be detected. Oxidation at 600°C

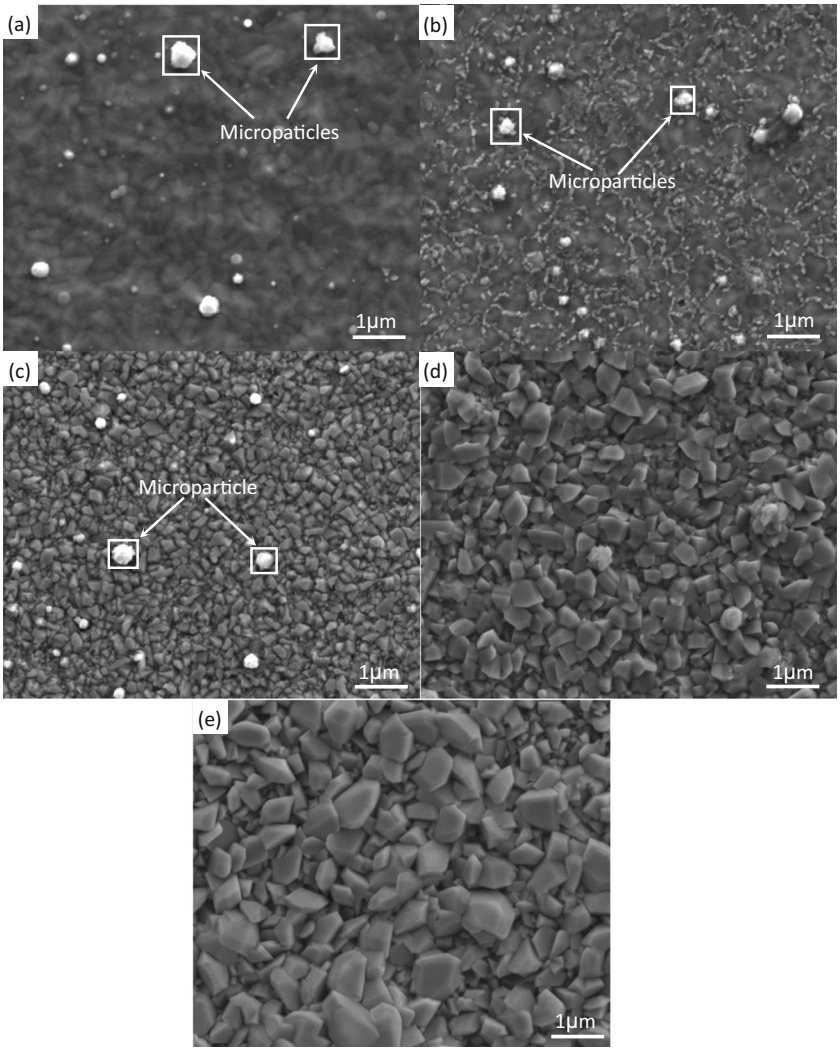

Figure 8: SEM surface micrograph of CrN coating A: (a) as deposited, (b) oxidized at 500°C, (c) oxidized at 600°C, (d) oxidized at 700°C and (e) oxidized at 800°C.

(Figure 9c) results in the generation of hexagonal chromium oxide Cr_2O_3 crystals with a size of 40–80 nm. Compared to coating A (Figure 9c), the oxide grains are finer and more uniform. Oxidation at 700°C (Figure 9d) results in a grain size of 100–500 nm and finally reached about 1,000 nm at 800°C (Figure 9e).

Summarizing it shows that in both cases oxide crystal grains are formed on the surfaces of both coatings at 500°C, but the oxide grains on the surface of coating B are not obvious. Higher oxidation temperatures let the oxide grains grow up, but grains formed on coating B at the same oxidation temperature are finer.

3.3 Corrosion resistance

The metal nitride film can provide a good corrosion protection for the substrate in most cases, but defects in the surface of the coating can decrease the corrosion resistance significantly. Different corrosion mechanisms are well known and described in the literature [31].

To investigate the effect of oxidation on the corrosion resistance of the coatings, electrochemical analysis before and after oxidation was carried out in an aqueous solution of 3.5 mass% NaCl at different temperatures. The dynamic potential polarization curves under the open circuit potential are shown in Figure 10. As the substrates are connected as anode, atoms of the coating's surface – preferentially from coating defects – will discharge ions and diffuse into the solution, thus generating a self-corrosion current [32]. The polarization curves were evaluated by Tafel linear extrapolation. The relevant corrosion data are presented in Table 3, where E_{corr} is the self-corrosion potential at the open circuit potential, J_0 is the self-corrosion current density and R_p is its corresponding polarization resistance.

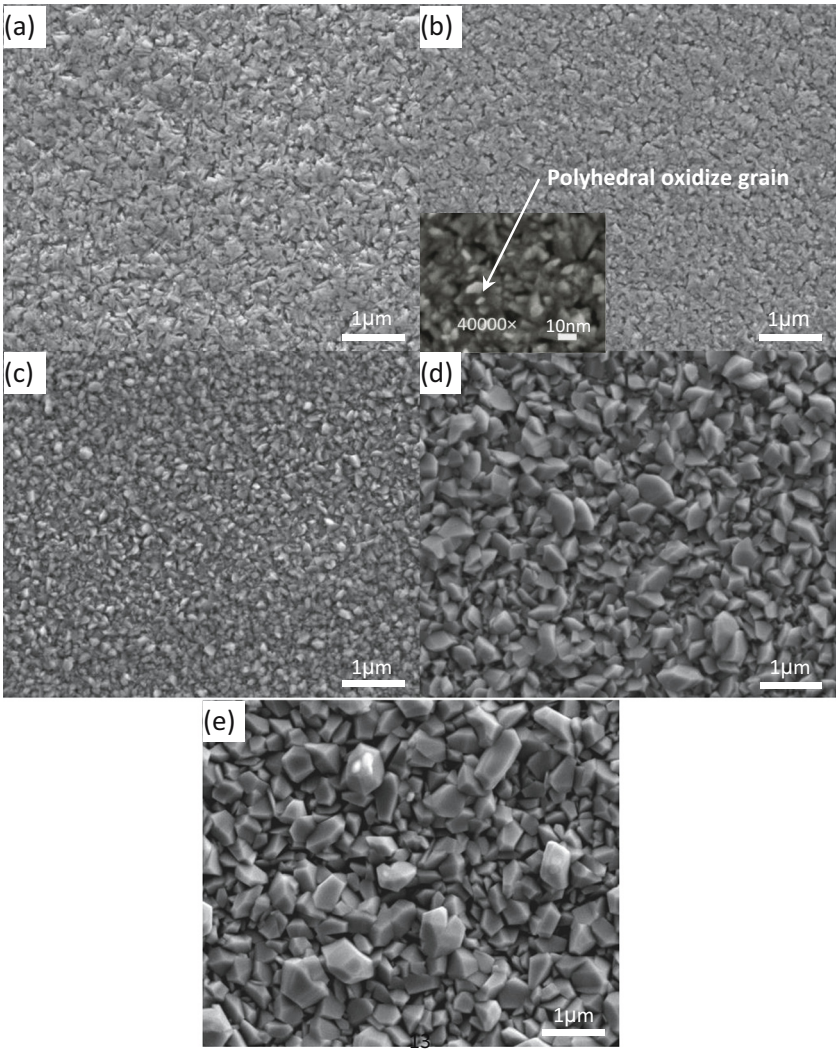

Figure 9: SEM surface micrograph of CrN coating B: (a) as deposited, (b) oxidized at 500°C, (c) oxidized at 600°C, (d) oxidized at 700°C and (e) oxidized at 800°C.

With the aim to better reflect the positive effect of the coating on improving the corrosion resistance of the substrate, the same electrochemical corrosion test was performed on 304 stainless steel substrates. The corrosion resistance of the substrate is much lower than that of the coating. At the same time, the polarization curve of the substrate is passivated at potentials of −0.69 and −0.31 V (Figure 10).

Table 3 states the following: coating A, as deposited, shows a corrosion potential (E_{corr}) of −0.278 V, a self-corrosion current density (J_0) of 3.467×10^{-7} A cm^{-2} and a polarization resistance (R_p) of 300.2 kΩ. After oxidation at 500°C, E_{corr} is decreased to −0.413 V, J_0 is increased to 5.402×10^{-7} A cm^{-2} and R_p is decreased to 265.2 kΩ. Due to the heterogeneity of the chemical composition and the heterogeneity of the structure, the meshwork of lighter line that composed of the chromium oxide (Figure 8b) on the surface of the coating will form a potential difference with the surrounding chromium nitride, thereby causing galvanic corrosion [32–34]. This increases the activation energy of the surface and causes a negative shift in the corrosion potential.

After oxidation at 600°C, E_{corr} of the coating is −0.363 V, which is positively shifted compared to that at 500°C, but still lower than E_{corr} of the as-deposited coating. The corresponding J_0 is reduced to 1.117×10^{-8} A cm^{-2} and R_p is increased to 2244.3 kΩ. From XRD and surface topography (Figures 6c and 7), it is known that the coating surface is covered with Cr_2O_3 in the shape of polyhedral particles. This increases the total areas of the surface, preventing penetration of the fluid into the interior of the coating, thus improving the corrosion resistance [35].

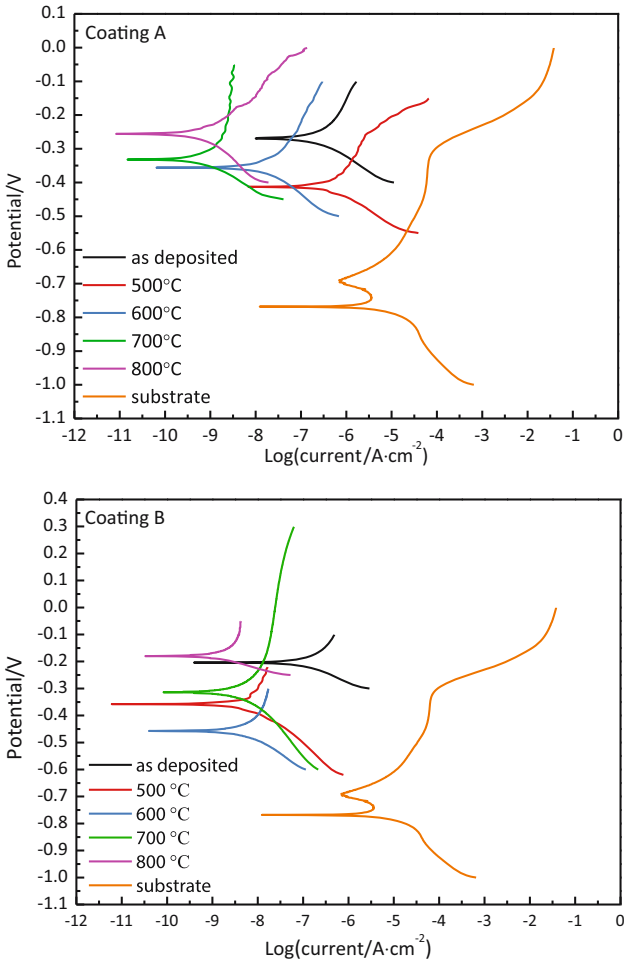

Figure 10: The polarization curves of coating A and coating B oxidized at different temperatures in 3.5% NaCl solution.

During oxidation at 700°C, the oxide particles on the surface of coating A formed a dense oxide film, which hinders the corrosion of the coating by Cl^- in the corrosion solution and makes it difficult to form corrosion holes, thus improving the corrosion resistance. This phenomenon is also reflected in the table data. The corrosion current density J_0 decreases and the polarization impedance R_p increases. Finally, oxidation at 800°C shifts E_{corr} to −0.256 V, lower than that of the as-deposited state. With that, J_0 decreased to 5.494×10^{-9} A cm^{-2} and the corresponding R_p increased to 5366.2 kΩ, leading to the conclusion that oxidation at 800°C results in the best corrosion resistance.

It is remarkable that – compared to the as-deposited state – oxidation at 500°C led to a decreased corrosion resistance with E_{corr} shifted negatively, increased J_0 and decreased R_p. But higher oxidation temperatures gradually increased corrosion resistance from 600 to 700°C and finally 800°C.

Coating B in the as-deposited state shows E_{corr} of −0.204 V, J_0 of 1.004×10^{-7} A cm^{-2} and R_p of 445.1 kΩ. This means that coating B – compared to coating A – is less corrosive. This can be explained by the rough surface of coating A with a high particle density and a small amount of pinholes, compared to the relatively smooth surface of coating B [33,36–39]. After oxidation at 500°C, E_{corr} decreased to −0.361 V, the polarization curve also shifted negatively, but J_0 decreased to 9.5×10^{-9} A cm^{-2}, and R_p increased to 4448.9 kΩ. This can be explained by the fact that there are no droplet particles on the surface of the coating, and the oxidation can take place uniformly (Figure 9b).

When the oxidation temperature increased to 600°C, E_{corr} resulted in −0.457 V, and a negative shift of the polarization curve occurred again. The results of XRD analysis (Figure 7), and the surface micromorphology (Figure 9c) shows that CrN, Cr_2N and Cr_2O_3 are present on the surface of the coating, resulting in heterogeneity of chemical composition and the structure of the coating. Therefore, at 500°C, galvanic corrosion is caused by the

Table 3: Fitting data of Tafel polarization curve after soaking in 3.5% NaCl solution for coatings A and B

Sample		E_{corr}/V_{SCE}	$J_0/(10^{-9}$ A cm$^{-2})$	$R_p/$(kΩ cm^{-2})
Coating A	As deposited	−0.278	346.7	300.2
	500°C	−0.413	540.2	265.2
	600°C	−0.363	11.2	2244.3
	700°C	−0.338	8.4	4745.2
	800°C	−0.256	5.5	5366.2
Coating B	As deposited	−0.204	100.4	445.1
	500°C	-0.361	9.5	4048.9
	600°C	−0.457	8.8	4420.7
	700°C	−0.314	6.9	6104.8
	800°C	−0.181	2.4	12443.1
Substrate	—	−0.768	9,208	2.9

potential difference. While at 600°C, the number of these galvanic corrosion systems increases, thereby enhancing the surface activity of the coating. Thus, the corrosion potential is negatively shifted.

As the oxidation temperature increased to 700°C, the oxide particles on the surface of the coating B increased, the oxide layer became thicker. As a result, the surface composition becomes uniform and the potential difference of the coating's surface gradually disappears, causing the corrosion potential shift positively.

After oxidation at 800°C, the surface of the coating was coated with a very corrosion-resistant Cr_2O_3 phase (Figure 9e), E_{corr} was changed to −0.181 V, lower than the as- deposited state, and J_0 was reduced to 2.414×10^{-9} A cm^{-2}. R_p was increased to 12443.1 kΩ. In summary, during oxidation of coating B, as the temperature increases, J_0 decreases, R_p increases and the corrosion resistance of the coating is improved. Starting from 700°C, the corrosion potential will gradually move to the positive axis [40,41].

It can be seen that with increasing oxidation temperature, the surface composition and the structure of the coating will change, leading to an obvious change in corrosion potential. However, the direct reason for the increase in corrosion resistance of the coating is the decrease in the self-corrosion current density. Therefore, the self-corrosion current density is more convincing in evaluating the corrosion resistance of the coating. Comparing the corrosion patterns of the two groups after oxidation, it was found that the corrosion resistance of coating B after oxidation at 800°C was the best.

4 Conclusions

In this study, the microstructure, surface morphology, adhesion strength and corrosion resistance of CrN/Cr multilayer coatings – prepared by arc evaporation and high power impulse magnetron sputtering – before and after oxidation at different temperatures were investigated. The obtained conclusions are as follows:

1. Both multilayer CrN/Cr coatings show thicknesses of 3.5 and 3.6 μm, respectively. The results of indentation test show that the bonding strengths of both coatings meet the requirements, and the HIPIMS coating performed even better.
2. SEM analysis reveals that many defects, such as pits and particles, appear on the surface of the arc evaporated coating in contrast to the surface of the HIPIMS coating that is smooth and flat. XRD-EDX results show that both coatings contain CrN, Cr and Cr_2N with small residual stress.
3. XRD-EDX shows that with increasing oxidation temperature, the amount of Cr_2N increases and of CrN decreases. Cr_2O_3 begins to form at 700°C. The analysis of the micromorphology surface reveals that both coatings are not oxidized to the same extent below 700°C. After oxidation at 800°C, both surfaces are covered by polyhedral oxidized grains with a size of about 1,000 nm. Compared with AIP coating, the diffusion of O in HIPIMS coating is more difficult and the oxidation depth is shallower, and hence, HIPIMS coating provides better oxidation resistance.
4. Potentiodynamic polarization curves indicate that the HIPIMS coating has the better corrosion resistance in 3.5 mass% NaCl solution. Corrosion resistance of the arc evaporated coating is lower due to the structural defects. The oxidized samples show better corrosion resistance than the as-deposited samples, and the coatings oxidized at 800°C exhibited the best corrosion resistance.

Acknowledgments: This work was supported by the Chinese 02 Special Fund (Grand No. 2017ZX02408003), the Chinese 1000 Plan for High Level Foreign Experts (Grand No. WQ20154100278), the Innovative Research Team Program of Henan University of Science and Technology (Grant No. 2015XTD006), and the Natural Science Fund Cultivation Project of Henan Province (Grant No. 162300410087).

Conflict of interest: The authors declare no conflict of interest regarding the publication of this paper.

References

[1] Subramanian B, Prabakaran K, Jayachandran M. Influence of nitrogen flow rates on materials properties of CrNx films grown by reactive magnetron sputtering. Bull Mater Sci. 2012;35(4):505–11.
[2] Hu L, Qi W, Li Y. Coating strategies for atomic layer deposition. Nanotechnol Rev. 2017;6:527–47.
[3] Wang L, Gong SD, Yang CH, et al. Electrical resistivity optimization of diamond-like carbon thin film for electrical probe storage application. Nanotechnol Rev. 2016;5:461–6.
[4] Gekonde HO, Subramanian SV. Tribology of tool-chip interface and tool wear mechanisms. Surf Coat Technol. 2002;149:151–60.
[5] Gautier C, Machet J. Effects of deposition parameters on the texture of chromium films deposited by vacuum arc evaporation. Thin Solid Films. 1996;289:34–8.

[6] Ehiasarian AP, Munz WD, Hultman L, Helmersson U, Petrov I. High power pulsed magnetron sputtered CrNx films. Surf Coat Technol. 2003;163:267–72.
[7] Greczynski G, Jensen J, Hultman L. CrNx films prepared by DC magnetron sputtering and high-power pulsed magnetron sputtering: a comparative study. IEEE Trans Plasma Sci. 2010;38(11):3046–56.
[8] Sarakinos K, Alami J, Wuttig M. Process characteristics and film properties upon growth of TiOx films by high power pulsed magnetron sputtering. J Phys D Appl Phys. 2007;40(7):2108–14.
[9] Jin QL, Wang HD, Li GL, Zhang JJ, Liu JN. Microstructures and mechanical properties of TiN/CrN multilayer films. Rare Met Mater Eng. 2017;46(10):2857–62.
[10] Lin J, Sproul WD, Moore JJ, Chistyakov R, Abraham B. Structurally laminated CrN films deposited by multi pulse modulated pulsed power magnetron sputtering. Surf Coat Technol. 2011;206(7):1780–6.
[11] Song GH, Luo Z, Li F, Chen LJ, He CL. Microstructure and indentation toughness of Cr/CrN multilayer coatings by arc ion plating. Trans Nonferr Met Soc China. 2015;25(3):811–6.
[12] Lamastra FR, Leonardi F, Montanari R, Casadei F, Valente T, Gusmano G. X-ray residual stress analysis on CrN/Cr/CrN multilayer PVD coatings deposited on different steel substrates. Surf Coat Technol. 2006;200:6172–5.
[13] Anders A, Andersson J, Ehiasarian A. High power impulse magnetron sputtering: current–voltage–time characteristics indicate the onset of sustained self-sputtering. J Appl Phys. 2007;102(11):113303.
[14] Gilewicz A, Chmielewska P, Murzynski D, Dobruchowska E, Warcholinski B. Corrosion resistance of CrN and CrCN/CrN coatings deposited using cathodic arc evaporation in Ringer's and Hank's solutions. Surf Coat Technol. 2016;299:7–14.
[15] Heinke W, Leyland A, Matthews A, Berg G, Friedrich C, Broszeit E. Evaluation of PVD nitride coatings, using impact, scratch and Rockwell-C adhesion tests. Thin Solid Films. 1995;270(S1–2):431–8.
[16] Verein Deutscher Ingenieure Normen, VDI 3198, (1991), VDI verlag.
[17] Violano G, Demelio G, Afferrante L. A note on the effect of surface topography on adhesion of hard elastic rough bodies with low surface energy. J Mech Behav Mater. 2019;28(1):8–12.
[18] Awati VB, Kengangutti A. Surface roughness effect on thermohydrodynamic analysis of journal bearings lubricated with couple stress fluids. Nonlinear Eng. 2019;8:397–406.
[19] Qi ZB, Sun P, Zhu FP, Wu ZT, Liu B, Wang ZC, et al. Relationship between tribological properties and oxidation behavior of $Ti_{0.34}Al_{0.66}N$ coatings at elevated temperature up to 900°C. Surf Coat Technol. 2013;231:267–72.
[20] Xie Q, Fu ZQ, Wei X, Li XY, Yue W, Kang JJ, et al. Effect of substrate bias current on structure and properties of CrNx films deposited by plasma enhanced magnetron sputtering. Surf Coat Technol. 2019;365:134–42.
[21] Polcar T, Kubart T, Novak R, Kopecky L, Siroky P. Comparison of tribological behaviour of TiN, TiCN and CrN at elevated temperatures. Surf Coat Technol. 2005;193(1):192–9.
[22] Bobzin K, Bagcivan N, Immich P, Bolza S, Alamib J, Cremerb R. Advancement of a nanolaminated TiHfN/CrN PVD tool coating by a nano-structured CrN top layer in interaction with a biodegradable lubricant for green metal forming. J Mater Proc Technol. 2009;209:165–70.
[23] Polcar T, Martine R, Vítů T, Kopecký L, Rodriguez R, Cavaleiro A. High temperature tribology of CrN and multilayered Cr/CrN coatings. Surf Coat Technol. 2009;203(20):3254–9.
[24] Sarakinos K, Alami J, Konstantinidis S. High power pulsed magnetron sputtering: a review on scientific and engineering state of the art. Surf Coat Technol. 2010;204(11):1661–84.
[25] Kashkarov EB, Obrosov A, Sutygina AN, Uludintceva E, Mitrofanov A, Weib S. Hydrogen permeation and mechanical and tribological behavior of CrNx coatings deposited at various bias voltages on IN718 by direct current reactive sputtering. Coatings. 2018;8:66–77.
[26] Lin JL, Sproul WD, Moore JJ. Tribological behavior of thick CrN coatings deposited by modulated pulsed power magnetron sputtering. Surf Coat Technol. 2012;206:2474–83.
[27] Li MS, Feng CJ, Wang FH. Effect of partial pressure of reactive gas on chromium nitride and chromium oxide deposited by arc ion plating. Rare Met Mater Eng. 2007;36(z2):699–702.
[28] Rovere F, Mayrhofer PH. Impact of yttrium on structure and mechanical properties of Cr–Al–N thin films. J Vacuum Sci Technol A Vacuum Surf Films. 2007;25:1336–40.
[29] Braun R, Rovere F, Mayrhofer P, Leyens C. Environmental protection of g-TiAl based alloy Ti–45Al–8Nb by CrAlYN thin films and thermal barrier coatings. Intermetallics. 2010;18:479–86.
[30] Wu ZT, Qi ZB, Zhu FP, Liu B, Wang ZC. Influences of Y addition on mechanical properties and oxidation resistance of CrN coating. Phys Proc. 2013;50:150–5.
[31] Beliardouh NE, Bouzid K, Nouveau C, Tlili B, Walock MJ. Tribological and electrochemical performances of Cr/CrN and Cr/CrN/CrAlN multilayer coatings deposited by RF magnetron sputtering. Tribol Int. 2015;82:443–52.
[32] Sanché JE, Sanché OM, Ipaz L, Aperador W, Caicedo JC, Amaya C, et al. Mechanical, tribological, and electrochemical behavior of $Cr_{1-x}Al_xN$ coatings deposited by r.f. reactive magnetron co-sputtering method. Appl Surf Sci. 2010;256:2380–7.
[33] Song GL. Potential and current distributions of one-dimensional galvanic corrosion systems. Corros Sci. 2010;52:455–80.
[34] Xie ZW, Chen Q, Chen T, Gao X, Yu XG, Song H, et al. Microstructure and properties of nitrogen ion implantation/AlN/CrAlN/MoS_2-phenolic resin duplex coatings on magnesium alloys. Mater Chem Phys. 2015;160:212–20.
[35] Ma JL, Zhang Y, Qin CH, Ren FZ, Wang GX. Effects of polystyrene sulfonate/graphene and Mn_3O_4/graphene on property of aluminum (zinc)–air batteries. Int J Hydrogen Energy. 2020;45:13025–34.
[36] Gao SJ, Dong CF, Luo H, Xiao K, Pan XM, Li XG. Scanning electrochemical microscopy study on the electrochemical behavior of CrN film formed on 304 stainless steel by magnetron sputtering. Electrochim Acta. 2013;114:233–41.
[37] Wang HW, Stack MM, Lyons SB, Hovsepian P, Miinz WD. The corrosion behaviour of macroparticle defects in arc bond-sputtered

CrN/NbN superlattice coatings. Surf Coat Technol. 2000;126: 279–87.

[38] Hovsepian PEh, Reinhard C, Ehiasarian AP. CrAlYN/CrN superlattice coatings deposited by the combined high power impulse magnetron sputtering/unbalanced magnetron sputtering technique. Surf Coat Technol. 2006;201:(7)4105–10.

[39] Gilewicz A, Murzynski D, Dobruchowska E, Kwiatkowski J, Olik R, Ratajski J, et al. Wear and corrosion behavior of CrCN/CrN coatings deposited by cathodic arc evaporation on nitrided 42CrMo4 steel substrates. Protect Met Phys Chem Surf. 2017;53(2):312–21.

[40] Teng Y, Guo YY, Zhang M, Yang YJ, Huang Z, Zhou YW, et al. Effect of Cr/CrNx transition layer on mechanical properties of CrN coatings deposited on plasma nitrided austenitic stainless steel. Surf Coat Technol. 2019;367:100–7.

[41] Ruden A, Restrepo-Parra E, Paladines AU, Sequeda F. Corrosion resistance of CrN thin films produced by dc magnetron sputtering. Appl Surf Sci. 2013;270:150–6.